# A Low-Order Model of Dolphin Swimming Dynamics: Fluke Flexibility and Energetics

Enric Xargay<sup>1</sup>, Gabriel Antoniak<sup>2</sup>, Kira Barton<sup>3</sup>, and K. Alex Shorter<sup>2</sup>

Abstract—This work presents a first-principles, low-order model of the sagittal-plane swimming dynamics of a bottlenose dolphin. The model captures key features of cetacean swimming, namely lift-based propulsion, unsteady hydrodynamics, fluke flexibility, and body posture. The model is used to estimate steady-state swimming kinematics and kinetics at a range of speeds, which are then compared to published estimates from swimming animals.

#### I. INTRODUCTION

Efficient movement through water is important for biological and engineered systems alike. Cetaceans, an order which includes orcas, dolphins, and whales, use lift-based propulsion generated by oscillating a flexible lunate tail (fluke) through water. These animals are efficient swimmers across their range of thrust production, with propulsive efficiencies estimated to reach 0.90 and exceed 0.80 across their entire range of speeds [1]. As a reference, single-screw vessels may exhibit propulsive efficiencies as high as 0.85, but only in a narrow band about the design point.

Unfortunately, the mechanisms behind the efficient movement of underwater biological systems are not well understood. Cetaceans are difficult to study because they spend a significant portion of their time underwater and out of view. Further, hydromechanical forces, like propulsive thrust or drag acting on the moving body, are particularly difficult to measure directly in the marine environment.

Bio-logging tags that collect kinematic data (e.g., speed, acceleration, orientation, depth) are used to gather information about these animals and, in managed marine environments, cameras have been used to complement single-point tag measurements. Tag-based kinematic measurements of animal movement result in data from thousands of strokes and, yet, estimating mechanical work and power from these kinematic measurements is a challenging problem. For bottlenose dolphins, previous work has combined measured speed and kinematics of the fluke (amplitude, frequency, pitch angle) with hydrodynamic models to estimate external forces acting on the animals [2].

Another common approach has been to estimate energetic costs of transport using proxies such as *overall dynamic body acceleration* calculated from tag data [3]. This approach has

been developed and tested with terrestrial animals and freediving sea lions where direct measurements of metabolic cost via respirometry have been possible [4]. However, experimental validation of the relationship between acceleration, mechanical work, and energetic cost remains limited for free-swimming cetaceans [5], [6]. Without calibration (which is seldom possible on large marine animals), comparisons between individuals are unlikely to be accurate and extrapolation across different behaviors within an individual may not hold.

To overcome some of these limitations, our research efforts focus on the development of a model-based framework to investigate the cost of swimming locomotion. The framework is informed by work in the human-walking literature where metabolic costs during locomotion, derived from respirometry, are related to mechanical costs estimated using inverse dynamics [7]. Here, we present a first-principles, low-order model of the sagittal-plane swimming dynamics of a bottlenose dolphin, which will be central to the proposed framework by allowing us to generate estimates of locomotive costs directly from tag-based kinematic measurements. The model captures identified key features of cetacean swimming, namely lift-based propulsion, unsteady hydrodynamics, fluke flexibility, and body posture [2]; and seamlessly incorporates findings from previous research on odontocete cetaceans, including body morphometry, fluke morphology and elasticity, and swimming gait and stability [8]-[12].

# II. HYDROMECHANICAL MODEL

## A. Model overview

The animal is modeled as an articulated multibody dynamic system subject to hydrostatic, hydrodynamic, and gravitational forces. The body of the animal is represented as an open chain of four rigid bodies, namely head, torso, and anterior and posterior caudal peduncle, which are linked successively by three active joints; see Figure 1. The model assumes that the animal can enforce a desired dorsoventral bending profile, specified in terms of the relative angular

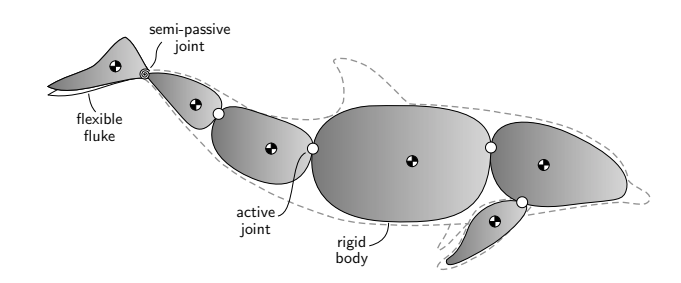


Fig. 1: Representation of the articulated multibody system.

¹Enric Xargay was a visiting scholar at the Department of Mechanical Engineering, University of Michigan, Ann Arbor, MI 48109 USA; e-mail: xargaycat@gmail.com

<sup>&</sup>lt;sup>2</sup>G. Antoniak and K. A. Shorter are with the Department of Mechanical Engineering, University of Michigan, Ann Arbor, MI 48109 USA; e-mail: {gjantoni,kshorter}@umich.edu

<sup>3</sup>K. Barton is with the Departments of Mechanical Engineering and

<sup>&</sup>lt;sup>3</sup>K. Barton is with the Departments of Mechanical Engineering and Robotics, University of Michigan, Ann Arbor, MI 48109 USA; e-mail: bartonkl@umich.edu

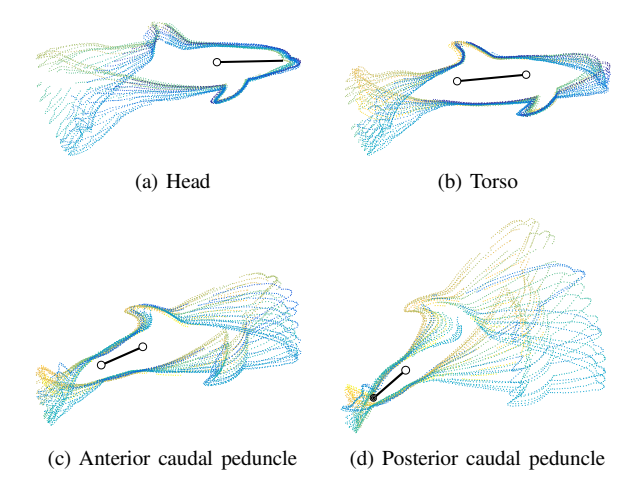


Fig. 2: Outlines of a *t. truncatus*, aligned by identified segments. (BL: 1.8 m; swimming speed: 2.1 BL/sec; frame rate: 60 fps.)

kinematics between adjacent elements of this body chain. The pectoral fins are also modeled as rigid bodies, which are linked by active spherical joints to the head element and act as hydrodynamic control surfaces. The fluke, on the other hand, is modeled as a semi-passive flexible element, which is connected to the posterior caudal peduncle element and whose deformation evolves in response to the hydrodynamic, elastic, and inertial forces acting on it. In turn, because the hydrodynamic loading over the fluke is affected by its deformation state, the model incorporates results from unsteady hydroelasticity to predict lift, drag, and pitchingmoment distributions over the deforming fluke.

The modeling approach places special emphasis on the adoption of techniques that significantly limit the computational complexity of the hydromechanical model, especially as it relates to the overall number of states and the use of online numerical quadrature. As a result, swimming dynamics are described by a finite set of nonlinear, highly coupled ordinary differential equations, with only tens of states. This results in a model with low computational complexity, especially when compared to full computational-fluid-dynamics simulation models (with millions of states) and models based on unsteady vortex-lattice methods (with thousands of states).

### B. Body

Segmentation of the body is based on analysis of video footage obtained during swim trials at various speeds; see Figure 2. The mass, volume, tensor of inertia, wetted surface area, location of the center of mass (CoM), and location of the center of buoyancy (CoB) of each body segment are estimated from orthogonal silhouettes using the approach described in [13], which is based on the assumption of superelliptical body cross-sections; see Figure 3. The four body segments are subject to added-mass and damping hydrodynamic forces and moments. In the setup adopted, the hydrodynamic axial force, normal force, and pitching moment acting on each body segment are determined from local flow properties using a quasi-steady hydrodynamic model.

The hydromechanical model runs a sinusoidal baseline dorsoventral bending profile, with constant phase shifts between successive joint deflections and speed-dependent gait

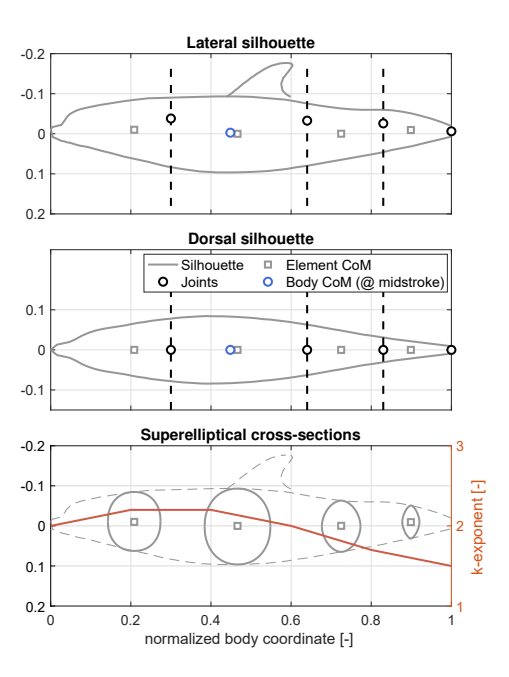


Fig. 3: Estimated center-of-mass (CoM) location of the four identified segments for a *t. truncatus* of 5.27 fineness ratio, obtained from orthogonal silhouettes [13].

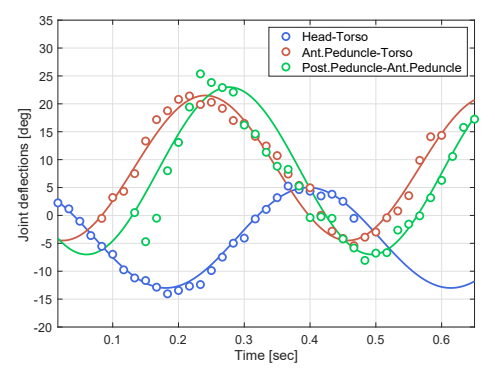


Fig. 4: Sinusoidal baseline dorsoventral bending profile (stroke cycle at  $2.1~\mathrm{BL/sec}$ ).

frequency and amplitude. This baseline profile has been identified from video footage obtained during swim trials at various speeds and is illustrated in Figure 4. The profile is qualitatively consistent with findings from previous studies, which identified out-of-phase movements of the rostrum relative to the peduncle to limit excessive transverse motions of the animal's head [8].

This baseline profile is augmented with corrective terms that, driven by feedback control laws, adjust the gait frequency and amplitude, as well as the relative angular kinematics of the caudal peduncle, to control the mean speed and the mean swim-path angle of the animal. More specifically, the joint deflections that describe the relative angular kinematics between adjacent body segments are of the form

$$\theta(V_{\rm ss}, t) = \bar{\theta}(t) + \Delta \theta(V_{\rm ss}, t) \sin(2\pi \zeta(t) + \varphi) , \quad (1)$$

where  $\zeta(t)$  is the 0-to-1 *stroke-cycle fraction*, defined as

$$\zeta(t) = \operatorname{frac}\left(\int_0^t \omega(V_{ss}, \tau) d\tau\right). \tag{2}$$

In expressions (1) and (2) above,  $\bar{\theta}$  is a bias term,  $\omega$  and  $\Delta\theta$  are, respectively, the angular frequency and amplitude of the gait's sinusoidal term, and  $\varphi$  is a constant phase shift. Gait frequency and amplitude depend on the target steady-state mean speed of the animal's CoM, denoted by  $V_{\rm ss}$ . Also, the explicit dependency on time, t, of the bias term, the gait frequency, and the gait amplitude indicates the presence of corrective terms adjusting these entities.

## C. Pectoral fins

Hydrodynamic forces on the pectoral fins are modeled using a nonlinear quasi-steady formulation capturing trailing-edge flow separation. The current inter-segment kinematic model assumes the pectoral fins are fixed with respect to the head element, at an orientation that minimizes resistance in the forward direction of travel. Therefore, the fins act as passive dampers that resist transverse recoil motions at the animal's head [8].

## D. Fluke Flexibility

The fluke is modeled as a flexible element, linked to the posterior caudal peduncle. To capture the effects of fluke flexibility on swimming performance, the model characterizes the fluke as a passive, flexible, thin plate that is linked to the caudal peduncle by a semi-passive joint at the "ball" caudal vertebra; see Figure 5. In this setup, the ball joint describes primary angular deformations of the fluke at its insertion onto the caudal peduncle, while thin-plate deflections account for secondary hydroelastic effects of chordwise and spanwise bending of the fluke blades. This characterization is consistent with existing physiological studies of bottlenose dolphins and minke whales, which conclude that most of the dorsoventral bending of flukes takes place at the intervertebral disk space immediately caudal to this vertebra [9], [14], [15].

Ball vertebra: The ball vertebra is modeled as a semipassive joint with a hardening torsion spring with asymmetric dorsoventral stiffness. The model assumes that the animal can actively adjust only the stiffness of this joint (not its deflection) and, hence, the motion of the joint is driven by hydrodynamic, elastic, and inertial forces. The semipassive nature of fluke deformation is supported by existing morphological studies [12], [17].

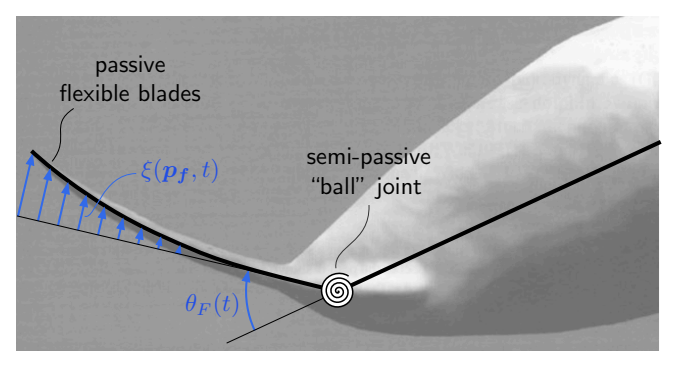


Fig. 5: Characterization of fluke flexibility. (Background image from [16, Fig. 6.7].)

Restricting deflections to the sagittal plane and letting  $\theta_F$  denote the deflection of the joint from its neutral position, the rotational dorsoventral stiffness of the ball joint is modeled as

$$\kappa_{\theta_F}(\omega, \theta_F) = u_{\kappa}(\omega) \, \kappa_{\theta_F}^0(\theta_F),$$

where  $\kappa^0_{\theta_F}(\theta_F)$  represents a nominal stiffness curve, and the factor  $u_\kappa(\omega)$  is used to actively modulate the stiffness of the ball joint in response to changes in the gait frequency. The nominal stiffness curve  $\kappa^0_{\theta_F}(\theta_F)$  is taken as the rotational stiffness of an asymmetric, hardening torsion spring, given by

$$\kappa_{\theta_F}^{0}(\theta_F) = \begin{cases} \kappa_{\mathrm{lin}}^{V} + \kappa_{\mathrm{qdr}}^{V} |\theta_F|, & \text{if } \theta_F \geq 0, \\ \kappa_{\mathrm{lin}}^{D} + \kappa_{\mathrm{qdr}}^{D} |\theta_F|, & \text{if } \theta_F < 0, \end{cases}$$

with  $\kappa^V_{\mathrm{lin}}, \kappa^V_{\mathrm{qdr}} > 0$  and  $\kappa^D_{\mathrm{lin}}, \kappa^D_{\mathrm{qdr}} > 0$  characterizing, respectively, ventral and dorsal bending of the ball joint. To meet experimental observations, the model assumes a larger stiffness for ventral bending than for dorsal bending.

Fluke blades: The fluke flexibility model also accounts for elastic bending of the fluke blades. Following standard aero- and hydroelastic formulations, the deformation of the fluke blades is represented by a linear superposition of assumed modes [18]:

$$\xi(\boldsymbol{p_f}, t) = \sum_{k=1}^{N_{\eta}} \Phi_k(\boldsymbol{p_f}) \, \eta_k(t) \,, \tag{3}$$

where  $\xi(\boldsymbol{p_f},t)$  denotes the transverse displacement at time t of the point of the fluke planform with spatial coordinates  $\boldsymbol{p_f}$ ;  $\Phi_k$  is the kth assumed mode;  $\eta_k$  is the generalized coordinate representing the amplitude of the kth assumed mode, and  $N_\eta$  is the total number of assumed modes retained in the modal expansion. With this setup, the deformation state of the fluke blades is described through a finite set of deformation variables  $\eta_k$ ,  $k=1,\ldots,N_\eta$ , characterizing the contribution of the various modes.

When using the assumed-modes method, the modal expansion must be carefully designed in order to avoid unnecessarily increasing both the order of the dynamics model and its numerical stiffness. In the current setup, the fluke-blade modes are approximated by free-vibration mode shapes of a partially pinned, orthotropic, rectangular plate. This approximation provides us with an analytical expression for the mode shapes, which is convenient for the computation of the modal terms in the fluke hydrodynamic model as well as in the derivation of the equations of motion.

Because the current model is limited to swimming dynamics in the sagittal plane, we can assume symmetry with respect to the root chord and derive the free-vibration mode shapes for the boundary-value problem illustrated in Figure 6. The governing differential equation for small amplitude free traverse vibration of an orthotropic, rectangular thin plate may be written as [19]

$$D_y \, \tfrac{\partial^4 \xi}{\partial \hat{y}_f^4} + 2 H \phi^2 \, \tfrac{\partial^4 \xi}{\partial \hat{x}_f^2 \, \partial \hat{y}_f^2} + D_x \phi^4 \left( \tfrac{\partial^4 \xi}{\partial \hat{x}_f^4} - \lambda^4 \xi \right) = 0 \,,$$

where  $\phi = b_{fluke}/(2\bar{c})$  is the plate aspect ratio, with  $\bar{c}$  being the mean chord of the fluke blades; H is the effective torsional rigidity;  $D_x$  and  $D_y$  are, respectively, the flexural

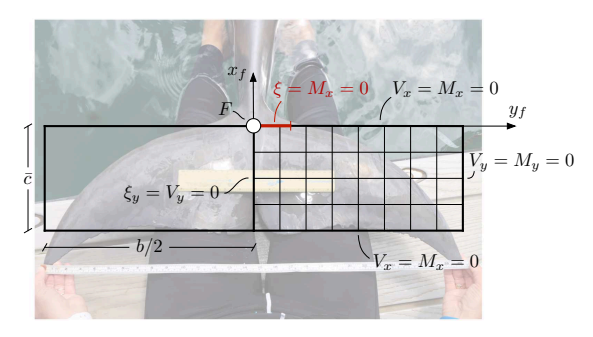


Fig. 6: Boundary conditions for a partially pinned, rectangular plate. (Background image courtesy of Dolphin Quest Oahu.)

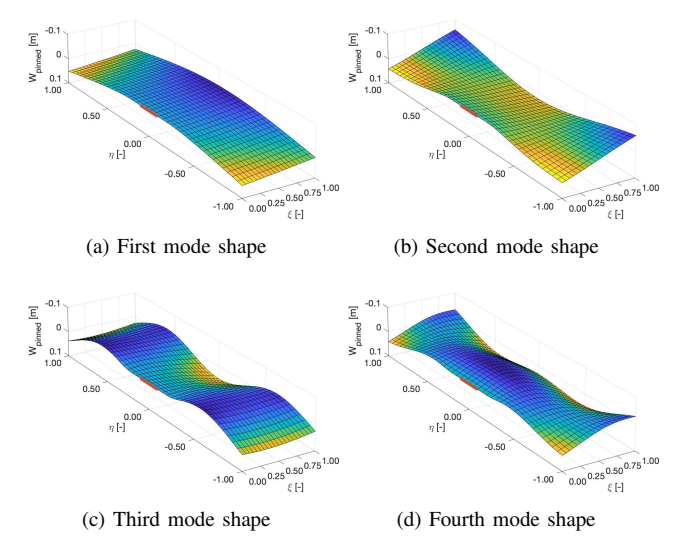


Fig. 7: Computed mode shapes for the first four modes of the partially pinned, orthotropic, rectangular plate.

rigidities associated with x- and y-directions;  $\lambda^2$  is the freevibration eigenvalue; and  $\hat{x}_f$  and  $\hat{y}_f$  are the normalized rectangular coordinates of the plate.

Analytical expressions for the mode shapes for this boundary-value problem have been obtained using the *su-perposition method*; see [20] and references therein. Figure 7 presents the first four mode shapes derived using this method.

# E. Fluke Hydrodynamics

To predict the unsteady hydrodynamic characteristics of the hydrofoil with due account of three-dimensional effects, we apply standard methods from lifting-line theory; see, for example, [21, §5.3.2] for a classical solution to the steadystate problem, and [22] for a modern numerical adaptation.

The procedure adopted in the present work can be summarized as follows. First, we assume a general unsteady circulation distribution along the hydrofoil's span and approximate it with a finite Fourier series expansion with time-varying Fourier coefficients:

$$\Gamma(\vartheta, t) = 2bV_{\perp} \sum_{n=1}^{N_{\Gamma}} A_n(t) \sin n\vartheta, \qquad (4)$$

where  $\vartheta$  is the spanwise Glauert angle, and  $V_{\perp}$  is defined as  $V_{\perp} = V_F \cos \Lambda_e$ , with  $V_F$  and  $\Lambda_e$  being, respectively, the speed of the ball vertebra and an effective sweep angle [23].

Then, we derive a spanwise loading equation and evaluate it at as many different spanwise stations as terms are included

in the Fourier series expansion. To this end, similar to [24], we assume that the sectional circulatory lift coefficient,  $c_l^{ef}$ , at any spanwise station satisfies the loading equation

$$c_l^{cf} = \frac{2}{V_{\perp}c}\Gamma + \frac{2}{V_{\perp}^2}\frac{\partial\Gamma}{\partial t}, \qquad (5)$$

where c represents the local section chord. Next, we choose  $N_{\Gamma}$  distinct spanwise collocation stations, and let  $y_m$  be the spanwise coordinate of one of these stations. We now approximate the sectional circulatory lift coefficient at the spanwise collocation station  $y_m$  of the fluke as

$$c_{l,m}^{cf} = c_{l_{\alpha},m} \left( \frac{1 + \sqrt{f_{\text{un},m}}}{2} \right)^2 (\alpha_{E,m} - \alpha_{l=0,m}) ,$$
 (6)

where  $c_{l_{\alpha},m}$  is the local sectional lift-curve slope,  $f_{\mathrm{un},m}$  is the local unsteady trailing-edge separation point<sup>1</sup>, and  $\alpha_{l=0,m}$  is the local angle of zero lift, which is a function of the deformation state of the fluke blades.

Remark 1: Let  $\eta = [\eta_1, \dots, \eta_{N_\eta}]^T$  be the vector of deformation variables characterizing the deformation state of the fluke blades. Then, following standard derivations in thinairfoil theory [26], it can be shown that the sectional angle of zero lift may be expressed as

$$\alpha_{l=0,m} = \boldsymbol{\lambda}_{\boldsymbol{\alpha}_1,m}^T \boldsymbol{\eta} + \frac{1}{V_{\perp}} \boldsymbol{\lambda}_{\boldsymbol{\alpha}_2,m}^T \dot{\boldsymbol{\eta}},$$

where  $\lambda_{\alpha_1,m}$  and  $\lambda_{\alpha_2,m}$  are vectors with components

$$\lambda_{\alpha_1, m_{(k)}} = \frac{1}{\pi} \int_0^{\pi} \Phi_k^x(\theta, y_m) (1 - \cos \theta) d\theta,$$
  
$$\lambda_{\alpha_2, m_{(k)}} = -\frac{1}{\pi} \int_0^{\pi} \Phi_k(\theta, y_m) (1 - \cos \theta) d\theta.$$

In these expressions,  $\Phi_k^x(\cdot) = \frac{\mathrm{d}\Phi_k}{\mathrm{d}x_f}(\cdot)$  is the derivative of the kth assumed mode with respect to the coordinate  $x_f$ , and the variable  $\theta$  is related to the coordinate  $x_f$  via the transformation  $x_f = -\frac{c}{2}(1-\cos\theta)$ . The key insight here is that vectors  $\lambda_{\alpha_1,m}$  and  $\lambda_{\alpha_2,m}$  can be pre-computed offline as soon as the assumed modes have been defined, and need not be re-computed as the simulation of the hydrodynamic model unfolds. As a result, the sectional angle of zero lift can be determined at an extremely low computational cost, without the need for online numerical quadrature.  $\triangle$ 

The local effective angle of attack,  $\alpha_{E,m}$ , is given by

$$\alpha_{E,m} = (1 - A_{\phi 1} - A_{\phi 2}) \left( \alpha_{3/4,m} - \alpha_{i,m} \right) + x_{\phi,m} , \quad (7)$$

where  $\alpha_{i,m}$  is the local induced angle of attack, and  $x_{\phi,m}$  is the local deficiency capturing the influence of trailingedge wake shedding. Borrowing from the work in [23], the induced angle of attack is approximated as

$$\alpha_{i,m} = \frac{\omega}{4\pi V_{\perp}} \int_{-b/2}^{b/2} \frac{\partial \Gamma/\partial y}{y_m - y} dy, \qquad (8)$$

where the downwash factor  $\omega$  is assumed to be independent of the spanwise coordinate and is given by [23, Eq. (89)]. The local deficiency is modeled as

$$\begin{split} x_{\phi,m} = & \sum_{j=1}^{2} \sum_{n=1}^{N_{\Gamma}} \kappa_{\phi j,mn} x_{\phi j,n} + \\ & \sum_{j=1}^{2} \sum_{n=1}^{N_{\Gamma}} A_{\phi j} \left( \delta_{mn} - \kappa_{\phi j,mn} \right) \left( \alpha_{3/4,n} - \alpha_{i,n} \right), \end{split}$$

<sup>&</sup>lt;sup>1</sup>The local unsteady trailing-edge separation point,  $f_{\text{un},m}$ , may be determined from an open-loop procedure similar to the one proposed in [25].

where  $x_{\phi j,n}$ , j=1,2, are deficiency states for the spanwise collocation station  $y_n$ ,  $\kappa_{\phi j,mn}$  are cross-coupling gains, and  $\delta_{mn}$  is the Kronecker delta. The deficiency states  $x_{\phi j,n}$ evolve according to the dynamics

$$\dot{x}_{\phi j,n} = -\frac{2V_{\perp}}{c_n} \left( b_{\phi j} + \frac{c_n \dot{V}_{\perp}}{2V_{\perp}^2} \right) x_{\phi j,n} + b_{\phi j} A_{\phi j} \frac{2V_{\perp}}{c_n} \left( \alpha_{3/4,n} - \alpha_{i,n} \right) ,$$

where  $A_{\phi 1}$ ,  $A_{\phi 2}$ ,  $b_{\phi 1}$ , and  $b_{\phi 2}$  are positive constants that

correspond to the coefficients of a second-order exponentialseries approximation of the Wagner indicial function [27]<sup>2</sup>. With this model, the states  $x_{\phi j,n}$ , j=1,2, track the twodimensional influence of the nth spanwise station's trailingedge wake shedding on itself, and the gains  $\kappa_{\phi j,mn}$  are used to capture three-dimensional effects.

From (5)–(8), it follows that the unsteady circulation distribution  $\Gamma$  must satisfy the following integro-differential equation at the spanwise collocation station  $y_m$ :

$$c_{l_{\alpha},m}^{f}\left(\left(1 - A_{\phi 1} - A_{\phi 2}\right)\left(\alpha_{3/4,m} - \frac{\omega}{4\pi V_{\perp}} \int_{-b/2}^{b/2} \frac{\partial \Gamma/\partial y}{y_{m} - y} \mathrm{d}y\right) + x_{\phi,m} - \alpha_{l=0,m}\right) = \frac{2}{V_{\perp} c_{m}} \Gamma_{m} + \frac{2}{V_{\perp}^{2}} \left(\frac{\partial \Gamma}{\partial t}\right)_{m},\tag{9}$$

where  $c_{l_{\alpha}}^{f} = c_{l_{\alpha}} \left( (1 + \sqrt{f_{\rm un}})/2 \right)^{2}$ . Using (4), equation (9) yields one differential equation that relates the unknown  $N_{\Gamma}$  Fourier coefficients,  $A_n$ , and their derivatives,  $\dot{A}_n$ . By combining the equations written at the  $N_{\Gamma}$  distinct spanwise collocation stations, we obtain a system of  $N_{\Gamma}$  independent differential equations, which can be expressed in compact form as

$$E\dot{x}_A = Ax_A + \frac{V_\perp}{4h}c_l$$

where  $oldsymbol{x_A} = [A_1, \dots, A_{N_\Gamma}]^T$  is the vector of Fourier coefficients, E and A are square matrices of order  $N_{\Gamma}$  with entries

$$\begin{split} \boldsymbol{E}_{(m,n)} &= \sin n\vartheta_m \,, \\ \boldsymbol{A}_{(m,n)} &= -\frac{2V_\perp}{c_m} \left(\frac{1}{2} + \frac{c_m\dot{V}_\perp}{2V_\perp^2}\right) \sin n\vartheta_m \\ &\quad -\frac{V_\perp}{4b} \, c_{l_\alpha,m}^f \left(1 - A_{\phi 1} - A_{\phi 2}\right) \omega \, n \frac{\sin n\vartheta_m}{\sin\vartheta_m} \,, \end{split}$$

and  $c_l$  is a vector whose mth component is given by

$$c_{l(m)} = c_{l_{\alpha},m}^{f} \left( \left( 1 - A_{\phi 1} - A_{\phi 2} \right) \alpha_{3/4,m} + x_{\phi,m} - \alpha_{l=0,m} \right).$$

The unsteady sectional lift coefficient may now be expressed as the sum of the sectional circulatory lift component and a sectional apparent-mass lift component:

$$c_{l} = \left(\frac{2}{V_{\perp}c}\Gamma + \frac{2}{V_{\perp}^{2}}\frac{\partial\Gamma}{\partial t}\right) + \pi \frac{c}{2V_{\perp}}\left(\frac{\dot{V}_{\perp}}{V_{\perp}}\left(\alpha_{1/2} - \bar{\alpha}\right) + \left(\dot{\alpha}_{1/2} - \bar{\alpha}_{d}\right)\right),$$

where  $\bar{\alpha}(y_f, \boldsymbol{\eta})$  and  $\bar{\alpha}_d(y_f, \dot{\boldsymbol{\eta}}, \ddot{\boldsymbol{\eta}})$  are terms that depend on the deformation state of the fluke blades.

Finally, the lift coefficient may be obtained via spanwise integration of this sectional lift coefficient, yielding

$$C_{L} \approx \pi \mathcal{R} A_{1} + \frac{\bar{c}}{2V_{\perp}} \kappa_{l_{0}}^{T} \left( \frac{\dot{V}_{\perp}}{V_{\perp}} x_{A} + \dot{x}_{A} \right)$$

$$+ \pi \frac{\bar{c}}{2V_{\perp}} \left( \frac{\dot{V}_{\perp}}{V_{\perp}} \left( \alpha_{1/2} - \kappa_{l_{1}}^{T} \boldsymbol{\eta} \right) + \left( \dot{\alpha}_{1/2} - \left( \kappa_{l_{1}}^{T} \dot{\boldsymbol{\eta}} + \frac{1}{V_{\perp}} \kappa_{l_{2}}^{T} \ddot{\boldsymbol{\eta}} \right) \right) \right),$$

$$(10)$$

where  $\mathcal{R}$  is the aspect ratio of the fluke, and  $\kappa_{l_0}$ ,  $\kappa_{l_1}$ , and  $\kappa_{l_2}$  are constant vectors with components

$$\begin{aligned} & \kappa_{l_0(n)} = 4\mathcal{R} \int_0^\pi \frac{c}{\bar{c}} \sin n\vartheta \sin \vartheta \, \mathrm{d}\vartheta \,, \\ & \kappa_{l_1(k)} = \frac{\mathcal{R}}{2\pi} \int_0^\pi \frac{c^2}{b\bar{c}} \sin \vartheta \int_0^\pi \Phi_k^x (1 - \cos 2\theta) \, \mathrm{d}\theta \, \mathrm{d}\vartheta \,, \\ & \kappa_{l_2(k)} = -\frac{\mathcal{R}}{2\pi} \int_0^\pi \frac{c^2}{b\bar{c}} \sin \vartheta \int_0^\pi \Phi_k (1 - \cos 2\theta) \, \mathrm{d}\theta \, \mathrm{d}\vartheta \,. \end{aligned}$$

In expression (10), the approximate sign is used because the apparent-mass component of lift has been derived with the assumption that the geometric angle of attack at mid-chord and its time-derivative are constant along the fluke's span. We note that the first term in (10) corresponds to the steadystate lift coefficient from classical lifting-line theory; see [21, Eq. (5.53)]. Expressions analogous to (10) can be derived for the fluke's drag and pitching-moment coefficients.

# F. Equations of Motion

To describe the motion of the animal swimming through water, the model uses two sets of variables. A set of transport variables describes the position, velocity, and attitude of a (pseudo-)body axis reference frame attached to the torso of the animal. The deformation variables  $\theta_F$  and  $\eta$ , introduced earlier, describe the deformation state of the flexible fluke.

Similar to the work in [30], the derivation of the equations of motion follows a mixed Newtonian-Lagrangian approach. On one hand, the equations of motion for transport variables result from the generalized Newton-Euler equations:

$$m\left(a_O + \frac{\mathrm{d}^2 r_{OG}}{\mathrm{d}t^2}\right) = f$$
  
 $\frac{\mathrm{d}h_O}{\mathrm{d}t} + mr_{OG} \times a_O = m_O$ 

where O and G refer, respectively, to the origin of the (pseudo-)body axis reference frame and to the CoM of the animal. On the other hand, the equations of motion for the deformation variables are derived from the commonly used Lagrange equations [31, §2.8]:

$$\begin{array}{l} \frac{\mathrm{d}}{\mathrm{d}t} \frac{\partial \mathcal{T}}{\partial \dot{\theta}_F} - \frac{\partial \mathcal{T}}{\partial \theta_F} + \frac{\partial \mathcal{U}}{\partial \theta_F} = Q_{\theta_F} \\ \frac{\mathrm{d}}{\mathrm{d}t} \frac{\partial \mathcal{T}}{\partial \dot{\eta}_k} - \frac{\partial \mathcal{T}}{\partial \eta_k} + \frac{\partial \mathcal{U}}{\partial \eta_k} = Q_{\eta_k} \,, \qquad k = 1, \dots, N_{\eta} \,. \end{array}$$

Here, to derive the terms  $Q_{\eta_k}$ , we assume attached flow conditions and borrow from the work in [32] to describe the unsteady pressure distribution acting on the fluke blades.

<sup>&</sup>lt;sup>2</sup>The indicial formulation adopted assumes that the shed wake extends as a planar surface from the trailing edge downstream to infinity. Clearly, this assumption does not hold for cetacean swimming, in which the amplitude of fluke oscillations is of the same order of magnitude as the fluke mean chord; see [1, Fig. 2]. However, as postulated in [28] and validated in [29], indicial formulations are able to accurately predict the influence of the shed wake on unsteady lift, provided the wavelength of the vortex wake is large compared to the foil chord. According to the data reported in [1, Fig. 1], in the range from 0.5 to 2.3 BL/sec, the tail-beat wavelength is between five to ten times larger than the fluke chord for the cetacean species studied.

### G. Swimming Kinetics

This first-principles modeling approach enables us to analytically determine the joint torques and mechanical power required to enforce the dorsoventral bending profile. The model can thus be used to estimate overall positive and negative mechanical work, entities that can be directly related to metabolic cost [7].

#### III. RESULTS

The model was used to investigate steady state swimming over a wide range of speeds (0.5 to 2.3 BL/sec). Preliminary kinematic and kinetic results from a heuristically tuned model match published results well. In fact, steady-state kinematic characteristics obtained from the model are in good agreement with kinematic observations previously reported in the literature; see Figure 8. Additionally, estimates of swimming kinetics (e.g., mean drag coefficient) and swimming energetics (e.g., mean thrust power) are comparable, over a wide range of speeds, to estimates obtained from previous works on cetacean swimming performance.

Figure 9 presents representative profiles of the instantaneous fluke force and the internal joint torques required to move the body through one steady-state stroke cycle at  $1.5~\mathrm{BL/sec}$ . The vector representation of the fluke force is shown at the quarter-cord position as the fluke moves through the cycle, and is colored to indicate when the fluke

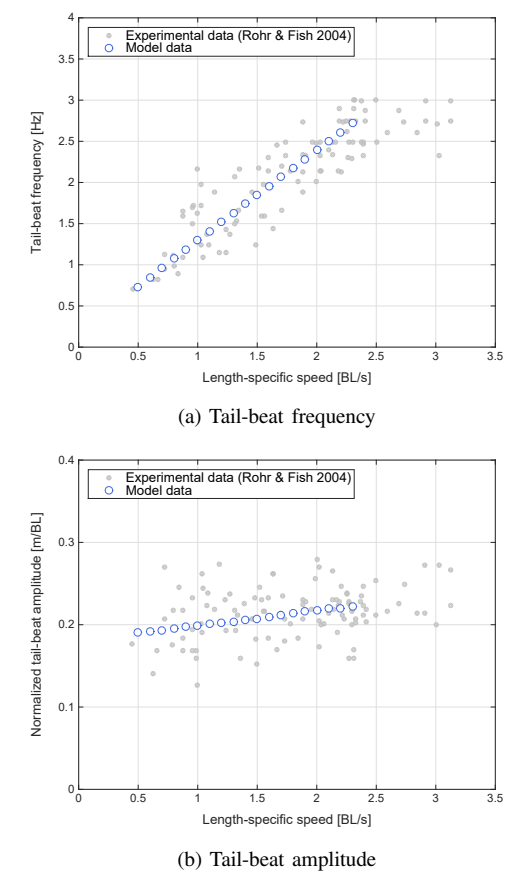
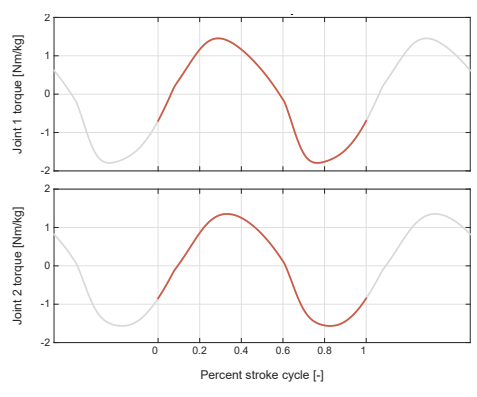
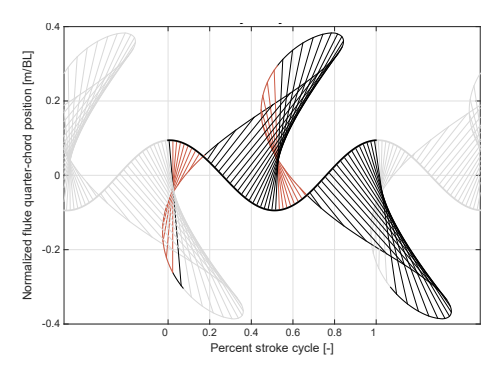


Fig. 8: Model results capture the relationship between tail-beat frequency, amplitude, and swimming speed that has been observed during swimming trials with bottlenose dolphins.



(a) Instantaneous joint torques



(b) Instantaneous fluke hydrodynamic force

Fig. 9: Results from steady-state simulations at 1.5 BL/sec. (9a) Estimated joint torques at the two peduncle joints; (9b) Resulting fluke force vectors (the aspect ratio of the force lines is 1:1; black lines indicate a positive contribution to forward thrust).

is generating propulsive (black) and drag (red) forces during swimming. Joint torques for the two peduncle joints are shown for the same cycle. Thrust force and joint torques, along with the angular velocities of the peduncle joints and the center of mass velocity, were used to calculate the summed joint and thrust power during swimming. The power estimates were then used to calculate estimated propulsive efficiency; see Figure 10. At slower speeds the efficiency was as high as 0.85, converging to 0.7 efficiency at the higher speeds. These results are lower than the estimates in [1], but comparable to the ones in [33].

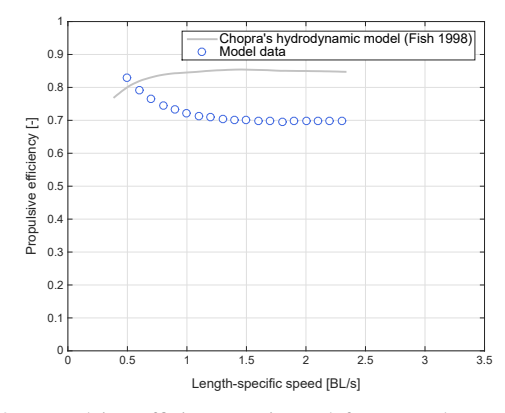


Fig. 10: Propulsive efficiency estimated from steady-state simulations of continuous swimming.

#### IV. CONCLUSIONS

This work presented a low-order hydromechanical model of the sagittal-plane swimming dynamics of a bottlenose dolphin. The model captures the effect on swimming performance of identified key features, including the animal's body posture, fluke hydroelasticity, and unsteady hydrodynamics with delayed fluke stalls. Additionally, the model has been designed to easily accommodate different body morphometrics, fluke morphology and elasticity, and gait profiles. As a result, the model represents a versatile tool that enables the investigation of cetacean swimming biomechanics, especially as it relates to the energetic cost of swimming. In particular, the model provides an opportunity to explore the limitations of single-body models, and the accuracy of energetic proxies derived from kinematic measurements.

More interestingly, the adopted modeling approach allows for an inverse dynamics analysis using kinematic data collected with a bio-logging tag. Preliminary work can be found in [34]. In this framework, the model is used to estimate the hydrodynamic, elastic, and inertial forces acting on an animal with set morphology during specific swimming trials, and to compute the work required to enforce the dorsoventral bending profile inferred from logged kinematic data. Furthermore, because of the low computational complexity of the model, the proposed framework enables the analysis of hundreds of hours of past and future logged swimming data.

# ACKNOWLEDGMENT

The authors would like to thank Frank Fish, Will Gough and Danielle Adams for their contributions to this work.

#### REFERENCES

- F. E. Fish, "Comparative kinematics and hydrodynamics of odontocete cetaceans: Morphological and ecological correlates with swimming performance," *Journal of Experimental Biology*, vol. 201, pp. 2867– 2877, October 1998.
- [2] F. E. Fish and J. J. Rohr, "Review of dolphin hydrodynamics and swimming performance," Tech. Rep. 1801, SPAWAR Systems Center, San Diego, CA, August 1999.
- [3] R. P. Wilson, C. R. White, F. Quintana, L. G. Halsey, N. Liebsch, G. R. Martin, and P. J. Butler, "Moving towards acceleration for estimates of activity-specific metabolic rate in free-living animals: the case of the cormorant," *Journal of Animal Ecology*, vol. 75, pp. 1081–1090, September 2006.
- [4] R. P. Wilson, L. Börger, M. D. Holton, D. M. Scantlebury, A. Gómez-Laich, F. Quintana, F. Rosell, P. M. Graf, H. Williams, R. Gunner, L. Hopkins, N. Marks, N. R. Geraldi, C. M. Duarte, R. Scott, M. S. Strano, H. Robotka, C. Eizaguirre, A. Fahlman, and E. L. C. Shepard, "Estimates for energy expenditure in free-living animals using acceleration proxies: A reappraisal," *Journal of Animal Ecology*, vol. 89, pp. 161–172, January 2020.
- [5] J. M. van der Hoop, A. Fahlman, T. Hurst, J. Rocho-Levine, K. A. Shorter, V. Petrov, and M. J. Moore, "Bottlenose dolphins modify behavior to reduce metabolic effect of tag attachment," *Journal of Experimental Biology*, vol. 217, pp. 4229–4236, December 2014.
- [6] A. S. Allen, A. J. Read, K. A. Shorter, J. Gabaldon, A. M. Blawas, J. Rocho-Levine, and A. Fahlman, "Dynamic body acceleration as a proxy to predict the cost of locomotion in bottlenose dolphins," *Journal of Experimental Biology*, vol. 225, February 2022.
- [7] B. R. Umberger and P. E. Martin, "Mechanical power and efficiency of level walking with different stride rates," *Journal of Experimental Biology*, vol. 210, pp. 3255–3265, July 2007.
- [8] F. E. Fish, J. E. Peacock, and J. J. Rohr, "Stabilization mechanism in swimming odontocete cetaceans by phased movements," *Marine Mammal Science*, vol. 19, pp. 515–528, July 2003.
- [9] F. E. Fish, M. K. Nusbaum, J. T. Beneski, and D. R. Ketten, "Passive cambering and flexible propulsors: cetacean flukes," *Bioinspiration & Biomimetics*, vol. 1, pp. S42–S48, December 2006.

- [10] F. E. Fish, J. T. Beneski, and D. R. Ketten, "Examination of the three-dimensional geometry of cetacean flukes using computed tomography scans: Hydrodynamic implications," *The Anatomical Record*, vol. 290, pp. 614–623, June 2007.
- [11] P. W. Weber, L. E. Howle, M. M. Murray, and F. E. Fish, "Lift and drag performance of odontocete cetacean flippers," *Journal of Experimental Biology*, vol. 212, pp. 2149–2158, July 2009.
  [12] D. S. Adams and F. E. Fish, "Odontocete peduncle tendons for possible
- [12] D. S. Adams and F. E. Fish, "Odontocete peduncle tendons for possible control of fluke orientation and flexibility," *Journal of Morphology*, vol. 280, pp. 1323–1331, September 2019.
- [13] R. Motani, "Estimating body mass from silhouettes: Testing the assumption of elliptical body cross-sections," *Paleobiology*, vol. 27, pp. 735–750, December 2001.
- [14] A. G. Watson and R. E. Fordyce, "Skeleton of two minke whales, Balaenoptera acutorostrata, stranded on the south-east coast of New Zealand," New Zealand Natural Sciences, vol. 20, pp. 1–14, September 1993.
- [15] W.-L. Tsai, "Dorsoventral bending of the tail and functional morphology of the caudal vertebrae in the bottlenose dolphin, *Tursiops truncatus*," Master's thesis, Oklahoma State University, Stillwater, OK, July 1998.
- [16] E. V. Romanenko, Fish and Dolphin Swimming. Russian Academic Monographs, Sofia, Bulgaria: Pensoft, 2002.
- [17] D. A. Pabst, "Intramuscular morphology and tendon geometry of the epaxial swimming muscles of dolphins," *Journal of Zoology*, vol. 230, pp. 159–176, May 1993.
- [18] R. L. Bisplinghoff, H. Ashley, and R. L. Halfman, Aeroelasticity. Mineola, NY: Dover Publications, 1996.
- [19] D. J. Gorman, "Accurate free vibration analysis of the completely free orthotropic rectangular plate by the method of superposition," *Journal of Sound and Vibration*, vol. 165, pp. 409–420, August 1993.
  [20] D. J. Gorman and S. D. Yu, "A review of the superposition method for
- [20] D. J. Gorman and S. D. Yu, "A review of the superposition method for computing free vibration eigenvalues of elastic structures," *Computers & Structures*, vol. 104–105, pp. 27–37, August 2012.
- [21] J. D. Anderson, Jr., Fundamentals of Aerodynamics. Series in Aeronautical and Aerospace Engineering, New York City, NY: McGraw-Hill, 2nd ed., 1991.
- [22] W. F. Phillips and D. O. Snyder, "Modern adaptation of Prandtl's classic lifting-line theory," *Journal of Aircraft*, vol. 37, pp. 662–670, July–August 2000.
- [23] D. Küchemann, "A simple method for calculating the span and chordwise loading on straight and swept wings of any given aspect ratio at subsonic speeds," Tech. Rep. ARC-RM-2935, Aeronautical Research Council, London, UK, August 1956.
- [24] M. Drela, "Integrated simulation model for preliminary aerodynamic, structural, and control-law design of aircraft," in AIAA Structures, Structural Dynamics and Materials Conference, (St. Louis, MO), pp. 1372–1383, April 1999. AIAA 1999-1394.
- [25] T. S. Beddoes, "Representation of airfoil behaviour," *Vertica*, vol. 7, no. 2, pp. 183–197, 1983.
- [26] J. Katz and A. Plotkin, Low-Speed Aerodynamics. Cambridge Aerospace Series, Cambridge, UK: Cambridge University Press, 2nd ed., 2001.
- [27] H. Wagner, "Über die Entstehung des dynamischen Auftriesbes von Tragflügeln," Zeitschrift für Angewandte Malhematik und Mechanik, vol. 5, pp. 17–35, February 1925.
- [28] J. O. Scherer, "Experimental and theoretical investigation of large amplitude oscillating foil propulsion systems," Tech. Rep. 662-1, Hydronautics, Inc., Laurel, MD, May 1968.
- [29] J. S. Izraelevitz, Q. Zhu, and M. S. Triantafyllou, "State-space adaptation of unsteady lifting line theory: Twisting/flapping wings of finitespan," AIAA Journal, vol. 55, pp. 2–16, April 2017.
- [30] G. Avanzini, E. Capello, and I. A. Piacenza, "Mixed Newtonian-Lagrangian approach for the analysis of flexible aircraft dynamics," *Journal of Aircraft*, vol. 51, pp. 1410–1421, September–October 2014.
- [31] L. Meirovitch, *Methods of Analytical Dynamics*. Advanced Engineering, New York, NY: McGraw-Hill, 1970.
- [32] C. O. Johnston, "Review, extension, and application of unsteady thin airfoil theory," Tech. Rep. 04–101, CIMSS, Virginia Polytechnic Institute and State University, Blacksburg, VA, August 2004.
- [33] F. Ayancik, K. W. Moored, and F. E. Fish, "Disentangling the relation between the planform shape and swimming gait in cetacean propulsion," in AIAA Fluid Dynamics Conference, (Atlanta, GA), June 2018. AIAA 2018-2914.
- [34] G. Antoniak, E. Xargay, J. Gabaldon, K. Barton, B.-I. Popa, and K. A. Shorter, "Estimating propulsive efficiency of bottlenose dolphins during steady-state swimming," in *Conference on Control Technology* and Applications, (Bridgetown, Barbados), August 2023.